A Transient SPICE Model for Dielectric-Charging Effects in RF MEMS Capacitive Switches

Xiaobin Yuan, *Member, IEEE*, Zhen Peng, *Student Member, IEEE*, James C. M. Hwang, *Fellow, IEEE*, David Forehand, *Member, IEEE*, and Charles L. Goldsmith, *Senior Member, IEEE*

***Abstract*—A transient simulation program with integrated circuit emphasis (SPICE) model for dielectric-charging effects in RF microelectromechanical system (MEMS) capacitive switches was developed and implemented in a popular microwave circuit simulator. In this implementation, the dielectric-charging effects are represented by R–C subcircuits with the subcircuit parameters extracted from directly measured charging and discharging currents in the picoampere range. The resulted model was used to simulate the actuation-voltage shift in switches due to repeated operation and dielectric charging. Agreement was obtained between the simulated and measured actuation-voltage shift under various control waveforms. For RF MEMS capacitive switches that fail mainly due to dielectric charging, the present SPICE model can be used to design control waveforms that can either prolong lifetime or accelerate failure.**

***Index Terms*—Accelerated life test, charging, dielectric, lifetime, microelectromechanical system (MEMS), reliability, RF, simulation program with integrated circuit emphasis (SPICE), switch, transient, trap.**

I. Introduction

In THE past decade, RF microelectromechanical system (MEMS) has emerged as a promising technology for low-loss switch, phase shifter, and reconfigurable network applications [1]–[4]. However, commercialization of RF MEMS devices is hindered by the need for continuing improvements in reliability and packaging. In particular, lifetime of electrostatically actuated RF MEMS capacitive switches is limited by dielectric-charging effects [5]. The dielectric is typically low-temperature-deposited silicon dioxide or nitride with a high density (10^{18} cm^{-3}) of traps associated with silicon dangling bonds. During switch operation, the electric field across the dielectric can be higher than 10^6 V/cm causing charge carriers to be injected into the dielectric and become trapped. With repeated operation, charge gradually builds up in the dielectric, which modifies the electrostatic force on the movable membrane resulting in an actuation-voltage shift [6].

Manuscript received April 13, 2006; revised July 19, 2006. This work was supported in part by the U.S. Air Force Research Laboratory under Contract F33615-03-C, which was funded by the U.S. Defense Advanced Research Projects Agency under the Harsh Environment, Robust Micromechanical Technology (HERMIT) Program. The review of this paper was arranged by Editor K. Najafi.

X. Yuan was with Lehigh University, Bethlehem, PA 18015 USA. He is now with the IBM Microelectronics Division, Hopewell Junction, NY 12533 USA (e-mail: xyuan@us.ibm.com).

Z. Peng and J. C. M. Hwang are with Lehigh University, Bethlehem, PA 18015 USA (e-mail: jh00@lehigh.edu).

D. Forehand and C. L. Goldsmith are with the MEMtronics Corporation, Plano, TX 75075 USA.

Digital Object Identifier 10.1109/TED.2006.882267

Dielectric-charging effects in RF MEMS have been studied by different research groups [5]–[20] with a qualitative charging model proposed [10]. In comparison, we have proposed an equation-based quantitative charging model to predict charge injection and actuation-voltage shift under dc stress conditions [13]. However, acceleration of charging effects under different control waveforms has not been characterized and modeled in detail. In addition, there has been no effort to implement a charging model in a commercial circuit simulator to help RF MEMS designers to quantify the charging effects and to optimize control waveforms. In this paper, we implement the equation-based charging model as equivalent circuits in a popular microwave circuit simulator ADS.[1] The equivalent-circuit model is then used in transient circuit simulation under various control waveforms. The results are in general agreement with that simulated by the equation-based model and the measured actuation-voltage shift. Therefore, for RF MEMS capacitive switches that fail mainly due to dielectric charging, the present model can be used to design control waveforms that can either prolong lifetime or accelerate failure. The present model complements existing equivalent-circuit models of MEMS switches, hence can be used to simulate the performance and reliability of circuits comprising multiple MEMS and electronic devices in the future.

II. Model Extraction

Fig. 1 illustrates a state-of-the-art metal–dielectric–metal RF MEMS capacitive switch fabricated on a glass substrate. The dielectric is sputtered silicon dioxide with a thickness of 0.25 μm and a dielectric constant of 4.0. The top electrode is a 0.3-μm-thick flexible aluminum membrane that is grounded. The bottom chromium/gold electrode serves as the center conductor of a 50-Ω coplanar waveguide for the RF signal. Without any electrostatic force, the membrane is normally suspended in air 2.5 μm above the dielectric. Control voltage with a magnitude of 20 V or higher is applied to the bottom electrode, which brings the membrane in contact with the dielectric, thus, forming a 120×80 μm capacitor to shunt the RF signal to ground. When the control voltage is reduced to below the release voltage of 8 V, the membrane springs back to its fully suspended position, resulting in little capacitive load to the RF signal. The switch has low insertion loss (0.06 dB) and adequate isolation (15 dB) at 35 GHz. The switching time is less than 10 μs.

[1] Agilent Technologies, Westlake Village, CA.

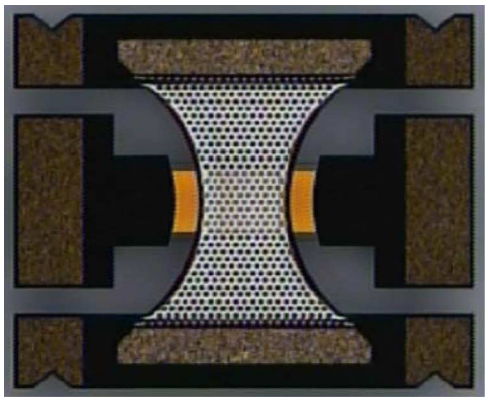

Fig. 1. Top view of a state-of-the-art RF MEMS capacitive switch. (Color version available online at http://ieeexplore.ieee.org.)

A charging model was constructed for the switch from the measured transient charging/discharging currents on the switch dielectric [13]. The total trapped charge density in the dielectric is modeled as

$$Q = \sum_J Q_J \left[1 - \exp(-t_{\rm ON}/\tau_{\rm CJ})\right] \exp(-t_{\rm OFF}/\tau_{\rm DJ}) \quad (1)$$

where Q_J is the steady-state charge density with charging and discharging time constants of $\tau_{\rm CJ}$ and $\tau_{\rm DJ}$, respectively. Usually, the charging and discharging phenomena can be characterized by two sets of time constants so that the summation needs to be carried over only two terms, i.e., $J = 1$ or 2. $t_{\rm ON}$ and $t_{\rm OFF}$ are the on and off times of the switch. Charging and discharging currents are expressed in the following:

$$I_C = A\frac{dQ}{dt} = A\sum_J \frac{Q_J}{\tau_{\rm CJ}} \exp(-t_{\rm ON}/\tau_{\rm CJ}) \quad (2)$$

$$I_D = A\frac{dQ}{dt} = -A\sum_J \frac{Q_J}{\tau_{\rm DJ}} \exp(-t_{\rm OFF}/\tau_{\rm DJ}) \quad (3)$$

where A is the surface area of the dielectric. From the measured charging and discharging transient currents, model parameters Q_J, $\tau_{\rm CJ}$, and $\tau_{\rm DJ}$ were extracted for different control voltages by fitting the measured data with exponential functions of (2) and (3). Two exponential functions were found to be sufficient for a good fit.

As shown in Fig. 2(a), the extracted charging and discharging time constants for both positive and negative control voltages exhibited no significant voltage dependence. Therefore, τ_C and τ_D were taken as the average value under different voltages. By contrast, the steady-state charge densities were found to vary exponentially with the control voltage, as illustrated in Fig. 2(b). The voltage dependence of the steady-state charge density is therefore modeled as

$$Q_J = Q_{0J} \exp(V/V_{0J}) \quad (4)$$

where V is the absolute value of the control voltage, and Q_0 and V_0 are fitting parameters. Using the above-described approach, two sets of model parameters were extracted for positive and negative control voltages, respectively, as listed in Table I. With the exponential voltage dependence, the magnitude of the voltage is limited to approximately twice the actuation voltage. Higher voltages may cause additional failure modes that are not relevant to switch lifetime under normal operating conditions.

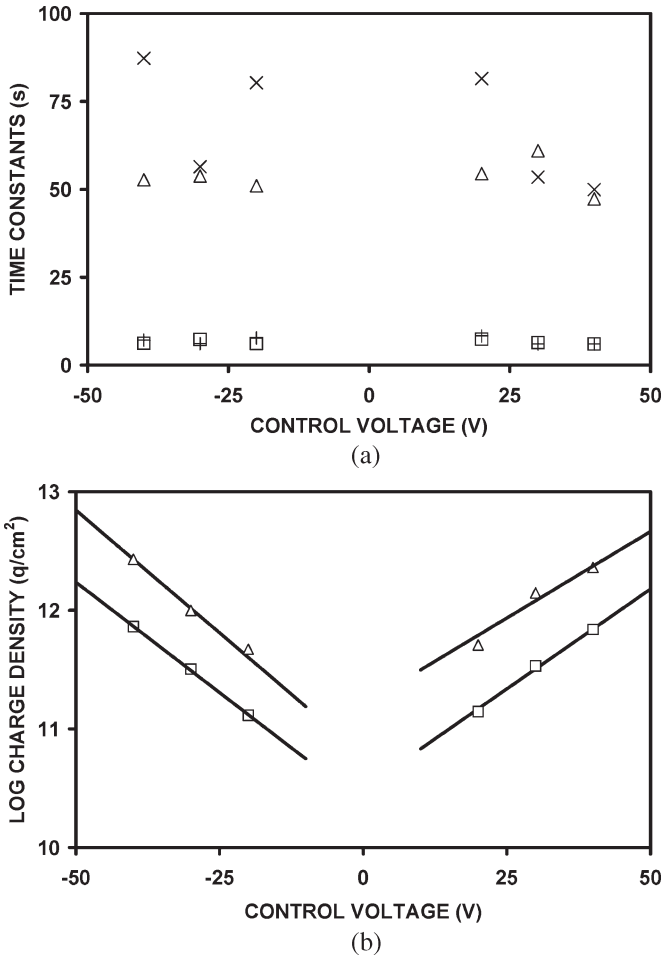

Fig. 2. (a) Type 1 (□) charging and (+) discharging and type 2 (△) charging and (x) discharging time constants. (b) (symbols) Extracted and (lines) fitted steady-state charge densities for (□) type 1 and (△) type 2 under −40, −30, −20, 20, 30, and 40 V. The time constants show no significant bias dependence, whereas the steady-state charge densities are exponentially dependent on the control voltage.

TABLE I
EXTRACTED MODEL PARAMETERS

Positive Bias				
J	τ_C(s)	τ_D(s)	Q_0 (q/cm^2)	V_0 (V)
1	6.6	6.8	3.1×10^{10}	13
2	54	62	1.6×10^{11}	15
Negative Bias				
J	τ_C(s)	τ_D(s)	Q_0 (q/cm^2)	V_0 (V)
1	6.5	7.0	2.4×10^{10}	12
2	53	75	6.0×10^{10}	11

The actuation-voltage shift due to the dielectric charging can be expressed as

$$\Delta V = hQ/\varepsilon_0\varepsilon_r \quad (5)$$

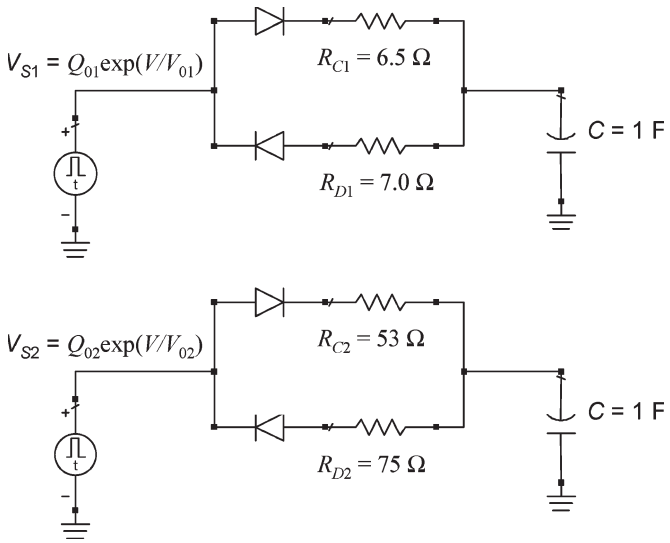

Fig. 3. ADS equivalent-circuit model for transient circuit simulation. Voltage dependence of the steady-state charge densities was implemented in the two voltage sources V_{S1} and V_{S2}. Diodes were used to direct the charge flow. $C = 1$ F, $R_{C1} = \tau_{C1}$, $R_{C2} = \tau_{C2}$, $R_{D1} = \tau_{D1}$, and $R_{D2} = \tau_{D2}$.

where h is the distance between the bottom electrode and the charge, Q is the charge density predicted by the charging model (1), ε_0 is the permittivity of free space, and ε_r is the relative dielectric constant. The charge is most likely distributed nonuniformly across the thickness of the dielectric. However, by approximating its collective effect on the actuation voltage with a charge sheet, it greatly simplifies the model. Since h cannot be directly measured, a single h value of 110 nm was found to give the best fit between model prediction and experimental data under all control waveforms. Approaches to calculate Q under complex control waveforms are illustrated in the following section.

III. Model Implementation

A. Equivalent-Circuit Model

In order to calculate the dielectric charge under complex control waveforms, the extracted charging model was implemented in ADS using an approach similar to that in [21]. As shown in Fig. 3, two R–C subcircuits were used to simulate charging and discharging of the dielectric. Both capacitances were set to unity so that the resistances correspond directly to the time constants: $R_{C1} = \tau_{C1}$, $R_{C2} = \tau_{C2}$, $R_{D1} = \tau_{D1}$, and $R_{D2} = \tau_{D2}$. Diodes in the subcircuits were used to direct charge flow. Therefore, the capacitor is charged through R_C during the switch-on time when the source voltage is larger than the capacitor voltage. Similarly, the capacitor discharges through R_D during the off time when the source voltage is smaller than the capacitor voltage. Total charge accumulated on unity capacitances represents total trapped charge in the dielectric. Voltage dependence of steady-state charge densities in (4) was implemented in two voltage sources. After defining the time-domain control waveform in the voltage sources, the dielectric charging and the actuation-voltage shift can be simulated using transient circuit simulation.

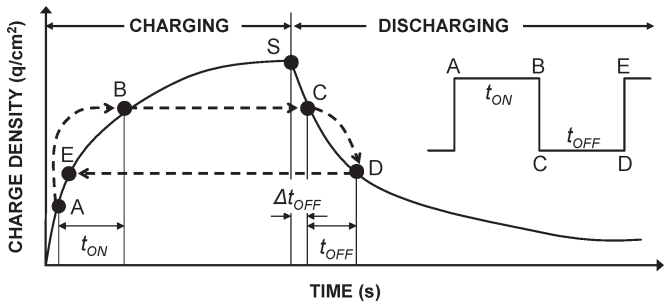

Fig. 4. Charging calculation under a square wave using the equation-based model. $t_{\rm ON}$ and $t_{\rm OFF}$ are the on and off times of the switch. After one operating cycle, the charge density increases from the initial-state A to the end-state E. Inset illustrates the applied square wave and the corresponding charging states.

B. Equation-Based Model

Another modeling approach [13] was used to calculate the charge injection under square-wave actuation. This is referred to as the equation-based model in contrast to the above-described equivalent-circuit model. Fig. 4 illustrates a charging curve that starts from the origin and ends in saturation (state S), which is followed by a discharging curve that falls exponentially according to the charging model (1). The charging and discharging curves shown in Fig. 4 are generated from the charging-model equations and can be expressed as in the following:

$$Q = \sum_J Q_J \left[1 - \exp(-t_{\rm ON}/\tau_{\rm CJ})\right] \tag{6}$$

$$Q = \sum_J Q_J \exp(-t_{\rm OFF}/\tau_{\rm DJ}). \tag{7}$$

During real switch operation under a square wave, the charging state at the beginning of each operating cycle can be somewhere between empty and full, such as state A illustrated on the charging curve. After the switch is turned on, the charging state moves higher to state B during the on time of the switch. After the switch is turned off, the dielectric starts to discharge from state C on the discharging curve, which is mapped horizontally from state B on the charging curve. After a certain off time, the dielectric is discharged to state D, which is then mapped back to state E on the charging curve to start the next operating cycle. Thus, the net effect of one operating cycle of the switch is to move the charging state from A to E. This equation-based charging/discharging model repeats in such a ratchet fashion until the desired number of cycles has been operated. To calculate charging under square waves, the model needs four input parameters: peak voltage, on time, off time, and number of cycles. Alternatively, on and off times can be specified in terms of frequency and duty factor of the waveform.

IV. Comparison With Measured Results

A. Accelerated Test Setup

Accelerated life tests for the switch shown in Fig. 1 were performed on a time-domain measurement setup [6]. A 6-GHz 10-dBm sinusoidal signal was applied to the switch input port together with the control waveform. RF output was sensed by

using a diode detector. Both the control and output waveforms were monitored by using an oscilloscope. First, a 0- to −30-V saw-tooth control wave was applied to the bottom electrode of a pristine (without any trapped charge in the dielectric) switch to sense the prestress actuation voltage. Next, the switch was stressed by applying a square or dual-pulse wave for different stress periods. After each stress period, another saw-tooth control wave was applied to the switch to sense the poststress actuation voltage. This way, the actuation-voltage shift for each stress period can be determined. Different stress waveforms were used to drive the switch in order to study the acceleration factors of the charging effects. Specifically, square waves with different peak voltages, duty factors, and frequencies were used, so were dual-pulse waveforms with different pull-down pulsewidths. Different stress experiments can be repeated on the same switch by restoring its pristine state with annealing at 120 °C for 1 h.

B. Square-Wave Actuation

Under a square control wave, the amount of charging within one operating cycle is determined by three parameters: peak voltage, duty factor, and frequency. We first investigate the effects of frequency and duty factor, while keeping the peak voltage constant. Specifically, the square wave used in Fig. 5 has an on voltage of −30 V and an off voltage of zero. The actuation voltage of the pristine switch is approximately −22 V at room temperature. Therefore, a peak voltage of −30 V ensures switch operation after significant actuation-voltage shift in either direction. A pristine switch was operated at two different frequencies: 10 and 100 Hz. Three duty factors were used at each frequency: 25%, 50%, and 75%.

After stressing the switch with the 0- to −30-V square wave for a certain period, the actuation voltage was shifted in the positive direction (less negative) indicating injection of electrons from the bottom electrode into the dielectric. An agreement was found between the simulated and the measured actuation-voltage shifts at both frequencies, as shown in Fig. 5. The simulation results from both equivalent-circuit and equation-based models are presented (difference between the two modeling approaches will be discussed at the end of this section). Both simulated and measured data suggest that for a fixed duty factor, the dielectric charging and actuation-voltage shift depend strongly on the total stress time instead of number of operating cycles. Notice that, for both frequencies, actuation-voltage shifts for the same stress period are very similar. So long as the stress frequency is much greater than the inverse of charging/discharging time constants, charge injection has no obvious dependence on the stress frequency. This is consistent with the experimental results in [10]. On the other hand, increasing the duty factor accelerates the dielectric charging and the actuation-voltage shift at both frequencies, as shown in Fig. 5. Fig. 5(c) shows a detailed view of the ADS-simulated actuation-voltage shift, which increases in a saw-tooth fashion through charging and discharging of the dielectric within each operating cycle.

For a given frequency, the on and off times within one operating cycle are determined by the duty factor. For the extreme case of dc stress (duty factor $= 100\%$), the charge density will eventually reach a saturated value $\sum Q_J$, which is implemented

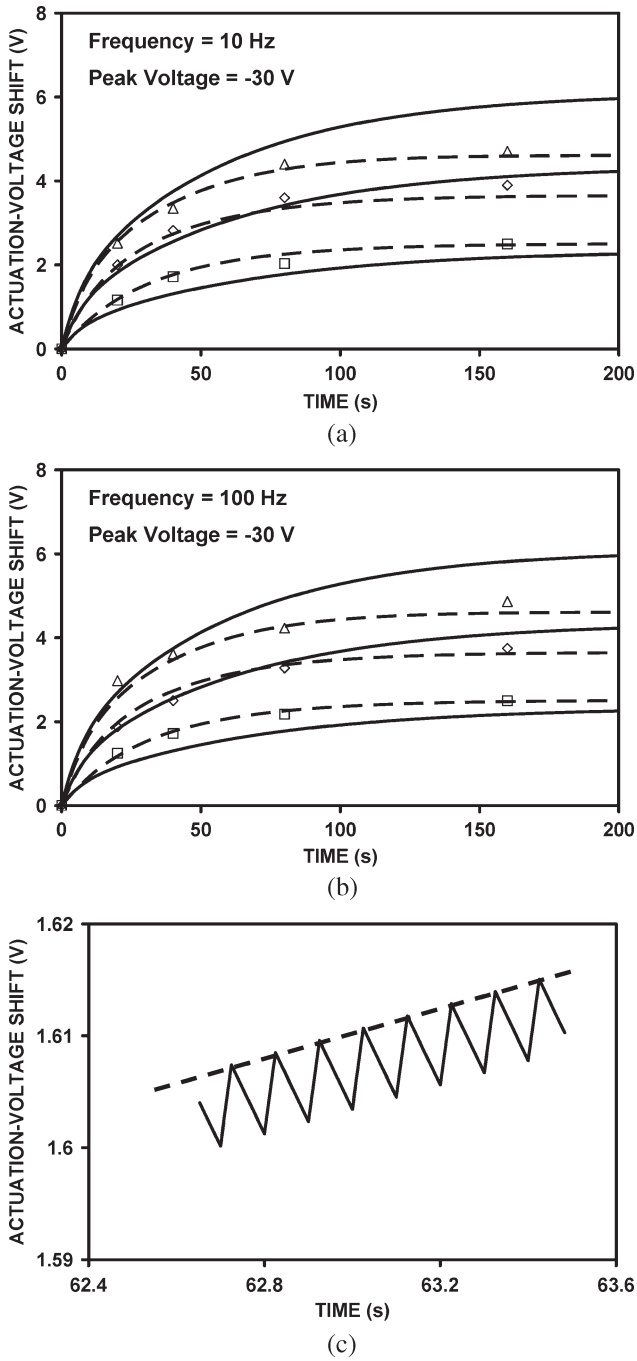

Fig. 5. Actuation-voltage shift as a function of stress time and frequency. The stress signal is a 0- to −30-V square wave at (a) 10 and (b) 100 Hz. Actuation-voltage shifts are simulated using (—) equivalent circuit and (- - -) equation-based models with 25%, 50%, and 75% duty factors bottom up. Measured actuation-voltage shifts are for (□) 25%, (◇) 50%, and (△) 75% duty factors. (c) Detailed view of the 25% duty-factor trace in (a) simulated by the equivalent-circuit model showing the charging and discharging dynamics of the dielectric. Dashed line represents the envelope of the charging/discharging transient. Both simulated and measured data show that, for the present test conditions, actuation-voltage shift is accelerated by duty factor but not by frequency.

in the voltage sources using (4). For an extremely low duty factor, such as 0.01%, the charge accumulated during the on time of the switch will be discharged almost completely during the off time; hence, little charge will ever be accumulated. An intermediate duty factor, e.g., 50%, will cause the charge

density to reach a steady-state value somewhere between 0 and $\sum Q_J$ when the charging and discharging processes are balanced. In a pristine switch, the charging rate is high to start with while the discharging rate is low. This builds up net charge so that charging slows down while discharging accelerates until charging and discharging are balanced. With the proper switch design and control waveform, it is possible to avoid switch failure even after the charging or actuation-voltage shift reaches a steady state. Therefore, the commonly quoted number of cycles before failure, due to its dependence on the detailed control waveform, is not a universal figure of merit for RF MEMS capacitive switches. For a square wave with a peak voltage that is defined by the actuation voltage, the frequency and duty factor must be specified for the quoted life cycles to be meaningful. Conversely, with the acceleration effects quantified through the present charging model, a fair comparison can be made between lifetimes measured under different frequencies and duty factors.

Empirically, it has been reported that the switch lifetime depends on the total on time and not on the duty factor or frequency of the control waveform. Our results in Fig. 5 also show that charging has no obvious dependence on the stress frequency. Using the present model, we show in the following analysis that this is only the limiting case when the switching period is much shorter than the charging/discharging time constants, and the total accumulated charge is much smaller than the saturated value $\sum Q_J$.

Consider the R–C subcircuits in Fig. 3. During the on time of an operating cycle, the capacitor is charged through R_C and the voltage accumulated on the capacitor after the on time is

$$V(t+t_{\rm ON}) = V_S\left[1-\exp(-t_{\rm ON}/\tau_C)\right]+V(t)\exp(-t_{\rm ON}/\tau_C) \tag{8}$$

where V_S is the source voltage, and $V(t)$ is the initial voltage on the capacitor before the on time starts. For clarity, the subscript "J" is temporarily omitted. During the off time of the operating cycle, the capacitance is discharged through R_D; the voltage (charge) left on the capacitor at the end of the off time is

$$V(t+t_{\rm ON}+t_{\rm OFF}) = V(t+t_{\rm ON})\exp(-t_{\rm OFF}/\tau_D). \tag{9}$$

Thus, (8) and (9) can be used iteratively to evaluate the charging state after ensuing operation cycles.

If $t_{\rm ON} \ll \tau_C$ and $t_{\rm OFF} \ll \tau_D$, (8) and (9) reduce to

$$V(t+t_{\rm ON}) \cong V_S\cdot t_{\rm ON}/\tau_C + V(t)(1-t_{\rm ON}/\tau_C) \tag{10}$$

$$V(t+t_{\rm ON}+t_{\rm OFF}) \cong V(t+t_{\rm ON})(1-t_{\rm OFF}/\tau_D). \tag{11}$$

Assuming a pristine capacitor without any charge at $t=0$, after the on time of the first operating cycle, the accumulated voltage given by (10) is

$$V(t_{\rm ON}) \cong V_S\cdot t_{\rm ON}/\tau_C. \tag{12}$$

The voltage left on the capacitor after the ensuing off time is given by (11) as

$$V(t_{\rm ON}+t_{\rm OFF}) \cong (V_S\cdot t_{\rm ON}/\tau_C)(1-t_{\rm OFF}/\tau_D). \tag{13}$$

Following the same procedure, the charge accumulation after the second on time is expressed as

$$V(2\cdot t_{\rm ON}+t_{\rm OFF}) \cong (V_S\cdot t_{\rm ON}/\tau_C) \cdot\left[1+(1-t_{\rm ON}/\tau_C)(1-t_{\rm OFF}/\tau_D)\right]. \tag{14}$$

Hence, charge accumulation after the nth on time is expressed as

$$V\left[n\cdot t_{\rm ON}+(n-1)t_{\rm OFF}\right] \cong (V_S\cdot t_{\rm ON}/\tau_C) \cdot\sum_{m=1}^{n}\left[(1-t_{\rm ON}/\tau_C)(1-t_{\rm OFF}/\tau_D)\right]^{m-1}. \tag{15}$$

After Taylor series expansion and dropping higher-order terms, (15) reduces to

$$V\left[n\cdot t_{\rm ON}+(n-1)t_{\rm OFF}\right] \cong (V_S\cdot t_{\rm ON}/\tau_C) \cdot\sum_{m=1}^{n}\left[1-(m-1)(t_{\rm ON}/\tau_C+t_{\rm OFF}/\tau_D)\right]. \tag{16}$$

After summing the arithmetical progression in (16) and dropping the insignificant terms, (16) is reduced to

$$\begin{aligned} &V\left[n\cdot t_{\rm ON}+(n-1)t_{\rm OFF}\right] \\ &\quad\cong \frac{V_S(n\cdot t_{\rm ON})}{\tau_C}\left[1-\frac{1}{2}\cdot\left(\frac{n\cdot t_{\rm ON}}{\tau_C}+\frac{n\cdot t_{\rm OFF}}{\tau_D}\right)\right] \\ &\quad\cong \frac{V_S(T\cdot P)}{\tau_C}\left\{1-\frac{1}{2}\cdot\left[\frac{T\cdot P}{\tau_C}+\frac{T\cdot(1-P)}{\tau_D}\right]\right\} \end{aligned} \tag{17}$$

where $T=n(t_{\rm ON}+t_{\rm OFF})$ is the total stress time, and $P=t_{\rm ON}/(t_{\rm ON}+t_{\rm OFF})$ is the duty factor. Therefore, when the frequency is high so that $t_{\rm ON} \ll \tau_C$ and $t_{\rm OFF} \ll \tau_D$, the charge injection is only affected by the total stress time and duty factor, but not by the frequency. In addition to the assumption of $t_{\rm ON} \ll \tau_C$ and $t_{\rm OFF} \ll \tau_D$, if we also assume that $n\cdot(t_{\rm ON}/\tau_C+t_{\rm OFF}/\tau_D) \ll 1$, (17) reduces to

$$V(T) = V_S(T\cdot P)/\tau_C \tag{18}$$

where $T\cdot P$ is the total on time. Therefore, when the switching period is much shorter than the charging/discharging time constants, and the total number of operated cycles is small so that the accumulated charge is much smaller than the saturated charge $\sum Q_J$, the trapped charge is proportional to the total on time, as has been observed.

It has been shown that increasing the peak voltage accelerates the charge injection and shortens the switch lifetime [5]. Voltage acceleration of dielectric charging was studied by using a 100-Hz 50% duty-factor square wave with -25-, -30-, and -35-V peak voltages. Both simulated and measured data in Fig. 6 confirm that increasing the peak voltage accelerates the dielectric charging resulting in larger actuation-voltage shifts at higher voltages. Since the peak voltage affects the steady-state charge densities but not the charging/discharging time constants, similar voltage acceleration can be expected for other frequencies and duty factors.

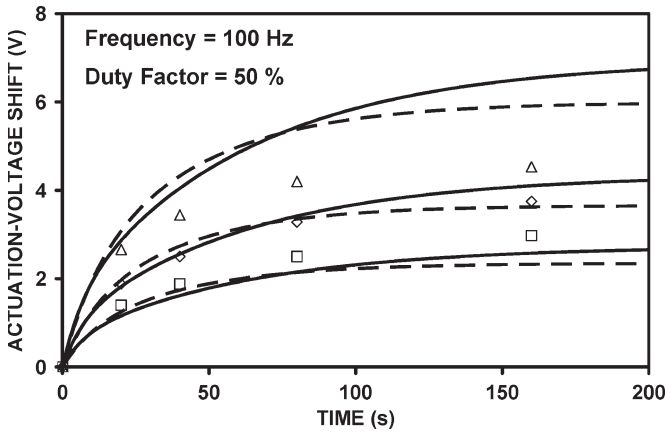

Fig. 6. Actuation-voltage shift as a function of stress time and peak voltage under a 100-Hz 50% duty-factor square wave. Actuation-voltage shifts are simulated using (—) equivalent circuit and (- - -) equation-based models with −25-, −30-, and −35-V peak voltages bottom up. Measured actuation-voltage shifts are for (□) −25-, (◇) −30-, and (△) −35-V peak voltages. Both simulated and measured data show that charging is accelerated by increasing the peak voltage.

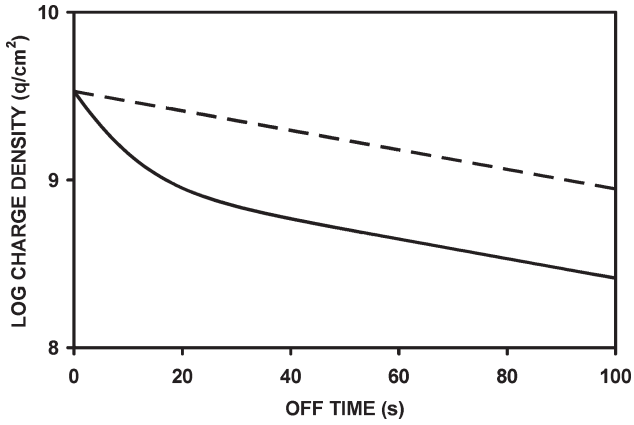

Fig. 7. Simulated charge density during the off time after a −30-V 50-ms on time using the (—) equivalent-circuit model and (- - -) equation-based model.

As shown by the measured and simulated results in Figs. 5 and 6, both equivalent-circuit and equation-based models predict that dielectric charging is accelerated by the duty factor and the peak voltage instead of operating frequency of the control waveform. However, when there are more than one set of time constants involved, subtle differences between the two modeling approaches arise. To examine such differences, we now sum over the subscript "J." Considering a pristine switch without trapped charge, after the first on time, the amount of trapped charge is determined by

$$V(t_{\rm ON}) = \sum_J V_{\rm SJ}\left[1 - \exp(-t_{\rm ON}/\tau_{\rm CJ})\right] \tag{19}$$

for both models. The charge after the ensuing off time is predicted by the equivalent-circuit model as

$$V(t_{\rm ON}+t_{\rm OFF}) = \sum_J V_{\rm SJ}\left[1 - \exp(-t_{\rm ON}/\tau_{\rm CJ})\right] \times \exp(-t_{\rm OFF}/\tau_{\rm DJ}). \tag{20}$$

On the other hand, by using the calculation routine illustrated in Fig. 4, the amount of charge during the ensuing off time is predicted by the equation-based model as

$$V'(t_{\rm ON}+t_{\rm OFF}) = \sum_J V_{\rm SJ}\exp[-(t_{\rm OFF}+\Delta t_{\rm OFF})/\tau_{\rm DJ}] \tag{21}$$

where the prime on V' indicates that it is calculated by the equation-based model. $\Delta t_{\rm OFF}$ is the time it takes for a full charge of $\sum V_{\rm SJ}$ to discharge to $V(t_{\rm ON})$, as illustrated in Fig. 4. Therefore, we have $V'(t_{\rm ON}) = \sum V_{\rm SJ}\exp(-\Delta t_{\rm OFF}/\tau_{\rm DJ}) = V(t_{\rm ON})$. This shows that both models predict same amount of charge at $t_{\rm OFF} = 0$. By contrast, the discharging rates for the two models are different. In other words, derivatives of (20) and (21) are different resulting in the difference between simulation results generated by the two models. The derivatives of (20) and (21) at $t_{\rm OFF} = 0$ can be expressed as

$$\frac{d\left[V(t_{\rm ON}+t_{\rm OFF})\right]}{dt_{\rm OFF}} = -\sum_J \frac{V_{\rm SJ}\left[1-\exp(-t_{\rm ON}/\tau_{\rm CJ})\right]}{\tau_{\rm DJ}} \tag{22}$$

$$\frac{d\left[V'(t_{\rm ON}+t_{\rm OFF})\right]}{dt_{\rm OFF}} = -\sum_J \frac{V_{\rm SJ}\exp(-\Delta t_{\rm OFF}/\tau_{\rm DJ})}{\tau_{\rm DJ}}. \tag{23}$$

Fig. 7 shows the comparison of the trapped charge during the off time predicted by the two models indicating the difference between (22) and (23). Although both models start with the same amount of charge, the equation-based model has a lower discharging rate and shows a more gradual decrease than the equivalent-circuit model. This causes a more aggressive charge accumulation using the equation-based model. As a result, Fig. 6 shows that the trapped charge calculated by using the equation-based model will start with a sharper increase and will reach steady state sooner than that simulated by using the equivalent-circuit model. The difference between the two discharging traces in Fig. 7 will diminish as the on time before discharging increases. For extremely long on times (e.g., 500 s), the traps are all charged to their steady-state values before the off time starts so that $\Delta t_{\rm OFF} = \exp(-t_{\rm ON}/\tau_C) = 0$, and (20) and (21) become the same. In addition, if there is only one set of charging and discharging time constants, (22) and (23) are essentially the same, and so are (20) and (21). However, when a more complicated control waveform is involved in the analysis, the calculation routine using the equation-based model is not as straight forward as the square-wave case. Therefore, the equivalent-circuit model will be advantageous in analyzing the dielectric charging under complex control waveforms such as dual-pulse waveforms discussed in the next section.

C. Dual-Pulse Actuation

A dual-pulse waveform has been proposed [5] to reduce charging by exploiting the difference between actuation and release voltages. The waveform comprises a short high-voltage pulse to quickly pull down the membrane and a low-voltage pulse to hold down the membrane for the remaining on time.

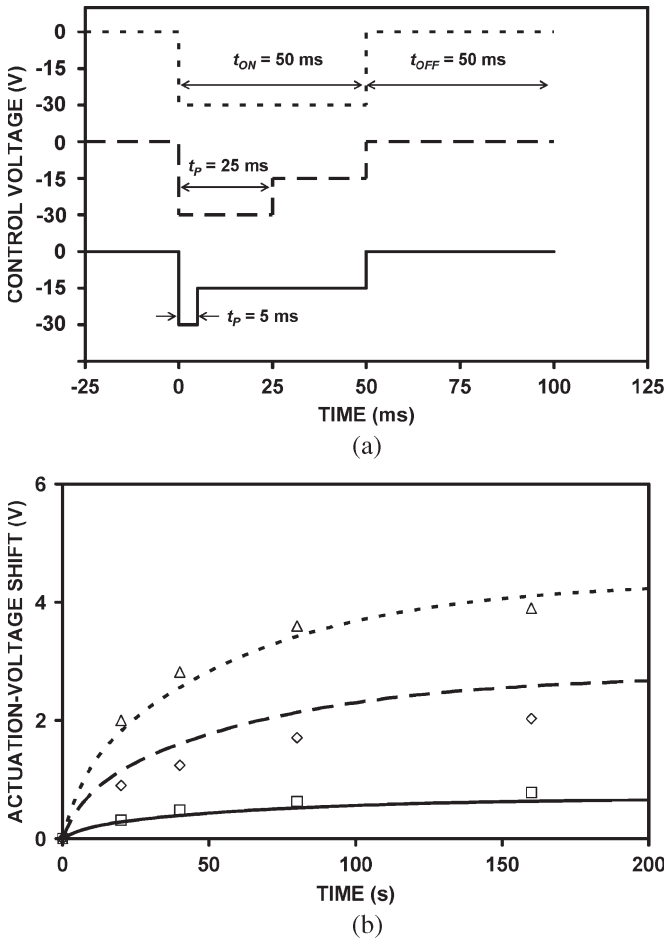

Fig. 8. (a) (—) dual pulse with $t_P = 5$ ms, (- - -) dual pulse with $t_P = 25$ ms, and $(\cdots)$ 0- to -30-V square waves used in the stress tests. The frequency is 10 Hz. Both square and dual-pulse waves have 50% duty factors. For the dual-pulse waves, the pull-down voltage is -30 V, and the hold-down voltage is -15 V. (b) Actuation-voltage shift as a function of stress time. ADS-simulated actuation-voltage shifts are for (—) dual pulse with $t_P = 5$ ms, (- - -) dual pulse with $t_P = 25$ ms, and $(\cdots)$ 0- to -30-V square wave. Measured actuation-voltage shifts are for (□) dual pulse with $t_P = 5$ ms, (◇) dual pulse with $t_P = 25$ ms, and (△) 0- to -30-V square wave. Charging is reduced by using the dual-pulse waves instead of the square wave.

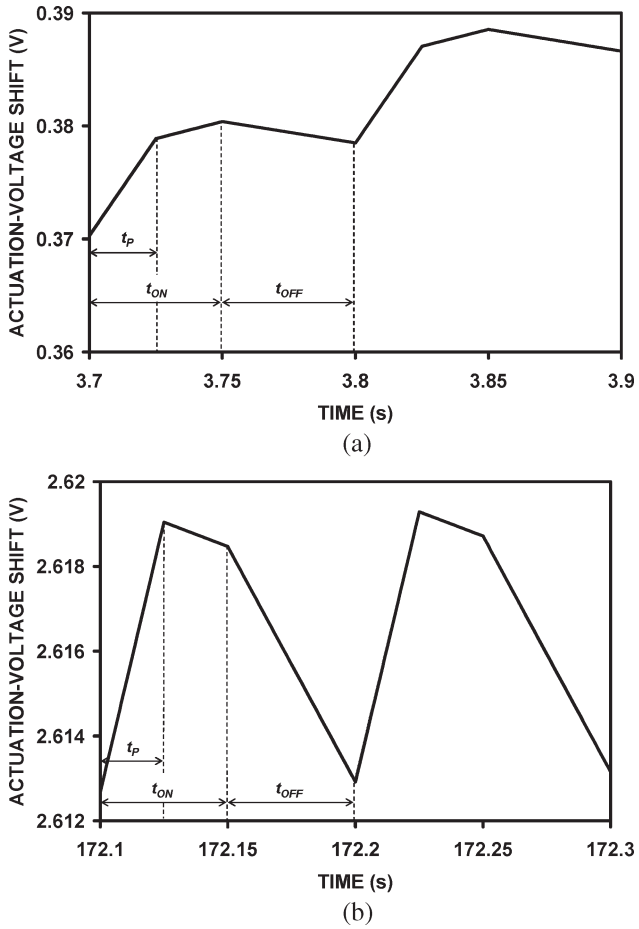

Fig. 9. ADS-simulated actuation-voltage shift as a function of stress time under a 10-Hz 50% duty-factor dual pulse with $t_P = 25$ ms. The pull-down voltage is -30 V, and the hold-down voltage is -15 V. (a) At the early stage of the stress period, the charge is injected for the entire on time, resulting in continuous increase of the actuation-voltage shift during the on time. (b) After the injected charge density exceeds the steady-state charge density defined by the hold-down voltage, the traps start to discharge for the hold-down period of the on time resulting in the decrease of the actuation-voltage shift during the period.

Thus, for most of the on time, the dielectric is subjected to the low-voltage hold-down pulse, and charging is reduced due to its exponential voltage dependence. As illustrated in Fig. 8(a), the dual pulse used in our measurement and simulation is a 10-Hz 50% duty factor $(t_{\rm ON} = t_{\rm OFF} = 50$ ms) signal. The pull-down voltage is -30 V, and the hold-down voltage is -15 V. The pull-down pulsewidth (t_P) was varied as a parameter. Comparing with the 0- to -30-V square wave, the dual-pulse waveforms reduced the charging significantly as expected. The present model can correctly predict the charging trend under such dual-pulse waveforms, as shown in Fig. 8(b).

Detailed charging/discharging dynamics for the dual-pulse waveforms are more complicated than the square-wave case shown in Fig. 5(c). The pull-down and hold-down voltages correspond to two different steady-state charge densities predicted by (4). For the dual-pulse waveform shown in Fig. 8(a), with $t_P = 25$ ms, detailed charging/discharging dynamics after different stress periods are shown in Fig. 9. At the beginning of the dual-pulse stress, the trapped charge starts with a sharp increase under the -30-V pull-down pulse, followed by a gradual increase for the rest of the on time under the -15-V hold-down pulse, then decreases during the off time, as shown in Fig. 9(a). As the charge builds up in the dielectric and exceeds the steady-state charge density defined by the hold-down voltage, the hold-down pulse is no longer able to inject charge into the dielectric. Therefore, the dielectric will discharge under the hold-down pulse causing the actuation-voltage shift to decrease during the hold-down period, as shown in Fig. 9(b). Thus, the charging/discharging dynamics is determined not only by the shape of the specific waveform (pull-down voltage and pulsewidth, hold-down voltage and pulsewidth, on and off times, etc.) but also by the charging state (how much charge has already accumulated).

V. Discussion

For the voltages applied in this paper, the steady-state charge density (Q_J) was found to depend exponentially on the voltage, while the charging and discharging time constants ($\tau_{\rm CJ}$ and $\tau_{\rm DJ}$) were found to be independent of the voltage. This suggests

that Q_J is not the density of traps, while $\tau_{\rm CJ}$ and $\tau_{\rm DJ}$ are not capture and emission times of traps. In fact, Q_J is of the order of 10^{11} q/cm^2, while the trap density is typically of the order of 10^{13} q/cm^2; $\tau_{\rm CJ}$ and $\tau_{\rm DJ}$ are of the order of seconds while trap capture and emission times are typically of the order of milliseconds. A recent study [20] also shows that Q_J increases with temperature while $\tau_{\rm CJ}$ and $\tau_{\rm DJ}$ are independent of temperature, which are not characteristic of a typical trap density and capture/emission times. Similar to the thermionic-emission-diffusion process across a Schottky barrier [22], charge injection into a dielectric is a rather complicated phenomenon. Initially, the charge-injection rate may depend on the voltage exponentially as we have observed. After a short time, the injected charge piles up in the dielectric and induces a retarding field to prevent further injection. Subsequent injection is possible only after the initially injected charge slowly diffuses further into the dielectric. Thus, Q_1 corresponds mainly to the amount of charge required to retard the initial injection, while τ_{C1} and τ_{D1} correspond mainly to the times required to inject and dissipate Q_1. Q_2, τ_{C2}, and τ_{D2} then characterize mainly the diffusion process. In-depth physical understanding of such a complicated phenomenon is the subject of current investigation and future publication.

Transient circuit simulation using the equivalent-circuit model in Fig. 3 can take hours to complete for high-frequency (e.g., 10 kHz) control waveforms. This is because the simulator tries to capture the full transient response (sawtooth-like charging/discharging dynamics as illustrated in Figs. 5(c) and 9) of the R–C circuits with long settling times. Using (8) and (9), the charge injection under square waves for certain stress period can be calculated iteratively. Within each operating cycle, the injected charge can be calculated at the end of the on time resulting in an envelope of the charging/discharging transient, as shown in Fig. 5(c). Thus, for high-frequency square waves, this iterative calculation routine is a much more efficient alternative to the transient circuit simulation in that it is capable of obtaining the envelope of the transient without having to capture the charging/discharging details within each operating cycle. However, when a more complex control waveform is used to drive the switch, a theoretical analysis can be more cumbersome making the equivalent-circuit model more favorable.

For RF MEMS capacitive switches whose lifetime is limited by dielectric charging, the present analysis shows that the number of operating cycles before failure is not a universal figure of merit. As shown in (17), as long as the stress frequency is much greater than the inverse of charging/discharging time constants, the charge injection is determined by the total stress time and duty factor instead of stress frequency or number of cycles. The peak voltage is also a critical acceleration factor, as shown in (4). These acceleration effects are experimentally verified and compared with the simulated results, as shown in Figs. 5 and 6. Therefore, control waveforms with high peak voltage, high duty factor, and low frequency can be used to accelerate failure. Conversely, control waveforms of low peak voltage, high frequency, and low duty factor may retard failure and result in improved lifetimes. In general, the peak voltage, frequency, and duty factor must be specified to allow fair comparison of switch lifetimes.

VI. Conclusion

A transient SPICE model for dielectric-charging effects in RF MEMS capacitive switches was developed and implemented in a commercially available circuit simulator ADS. The model was used to analyze charging and discharging under different control waveforms and was found to be in agreement with the experimental data. Both simulated and measured data show that dielectric-charging effects can be accelerated through duty factor and peak voltage of the control waveform, whereas frequency is not an acceleration factor. Therefore, for RF MEMS capacitive switches that fail mainly due to dielectric charging, the present model can be used to analyze and design control waveforms that can either prolong lifetime or accelerate failure. This transient SPICE model also makes it convenient to simulate circuits that comprise multiple MEMS and electronic devices in the future.

References

[1] C. L. Goldsmith, Z. Yao, S. Eshelman, and D. Denniston, "Performance of low-loss RF MEMS capacitive switches," *IEEE Microw. Guided Wave Lett.*, vol. 8, no. 8, pp. 269–271, Aug. 1998.

[2] D. Peroulis, S. Pacheco, K. Sarabandi, and L. P. B. Katehi, "MEMS devices for high isolation switching and tunable filtering," in *Proc. IEEE MTT-S Int. Microw. Symp. Dig.*, Jun. 2000, vol. 2, pp. 1217–1220.

[3] A. Malczewski, S. Eshelman, B. Pillans, J. Ehmke, and C. L. Goldsmith, "X-band RF MEMS phase shifters for phased array applications," *IEEE Microw. Guided Wave Lett.*, vol. 9, no. 12, pp. 517–519, Dec. 1999.

[4] G. M. Rebeiz, G.-L. Tan, and J. S. Hayden, "RF-MEMS phase shifters: Design and applications," *IEEE Microw. Mag.*, vol. 3, no. 2, pp. 72–81, Jun. 2002.

[5] C. L. Goldsmith, J. Ehmke, A. Malczewski, B. Pillans, S. Eshelman, Z. Yao, J. Brank, and M. Eberly, "Lifetime characterization of capacitive RF MEMS switches," in *Proc. IEEE MTT-S Int. Microw. Symp. Dig.*, Jun. 2001, vol. 1, pp. 227–230.

[6] X. Yuan, S. V. Cherepko, J. C. M. Hwang, C. L. Goldsmith, C. Nordquist, and C. Dyck, "Initial observation and analysis of dielectric-charging effects on RF MEMS capacitive switches," in *Proc. IEEE MTT-S Int. Microw. Symp. Dig.*, Jun. 2004, vol. 3, pp. 1943–1946.

[7] E. K. Chan, K. Garikipati, and R. W. Dutton, "Characterization of contact electromechanics through capacitance–voltage measurements and simulations," *J. Microelectromech. Syst.*, vol. 8, no. 2, pp. 208–217, Jun. 1999.

[8] J. R. Reid and R. T. Webster, "Measurements of charging in capacitive microelectromechanical switches," *Electron. Lett.*, vol. 38, no. 24, pp. 1544–1545, Nov. 2002.

[9] W. M. van Spengen, R. Puers, R. Mertens, and I. De Wolf, "Experimental characterization of stiction due to charging in RF MEMS," in *IEDM Tech. Dig.*, Dec. 2002, pp. 901–904.

[10] ——, "A comprehensive model to predict the charging and reliability of capacitive RF MEMS switches," *J. Micromech. Microeng.*, vol. 14, no. 4, pp. 514–521, Jan. 2004.

[11] D. Dubuc, W. M. van Spengen, S. Melle, I. De Wolf, R. Mertens, P. Pons, K. Grenier, and R. Plana, "Methodology to assess the reliability behavior of RF-MEMS," in *Proc. 34th Eur. Microw. Conf.*, Oct. 2004, pp. 61–64.

[12] X. Rottenberg, B. Nauwelaers, W. Raedt, and H. A. C. Tilmans, "Distributed dielectric charging and its impact on RF-MEMS devices," in *Proc. 34th Eur. Microw. Conf.*, Oct. 2004, pp. 77–80.

[13] X. Yuan, J. C. M. Hwang, D. Forehand, and C. L. Goldsmith, "Modeling and characterization of dielectric-charging effects in RF MEMS capacitive switches," in *Proc. IEEE MTT-S Int. Microw. Symp. Dig.*, Jun. 2005, pp. 753–756.

[14] S. Melle, D. De Conto, L. Mazenq, D. Dubuc, K. Grenier, L. Bary, O. Vendier, J. L. Muraro, J. L. Cazaux, and R. Plana, "Modeling of the dielectric charging kinetic for capacitive RF MEMS," in *Proc. IEEE MTT-S Int. Microw. Symp. Dig.*, Jun. 2005, pp. 757–760.

[15] G. J. Papaioannou, M. Exarchos, V. Theonas, G. Wang, and J. Papapolymerou, "On the dielectric polarization effects in capacitive RF-MEMS switches," in *Proc. IEEE MTT-S Int. Microw. Symp. Dig.*, Jun. 2005, pp. 761–764.

[16] ——, "Temperature study of the dielectric polarization effects of capacitive RF MEMS switches," *IEEE Trans. Microw. Theory Tech.*, vol. 53, no. 11, pp. 3467–3473, Nov. 2005.

[17] J. F. Kucko, J. C. Petrosky, J. R. Reid, and K. Yung, "Non-charge related mechanism affecting capacitive MEMS switch lifetime," *IEEE Microw. Wireless Compon. Lett.*, vol. 16, no. 3, pp. 140–142, Mar. 2006.
[18] R. W. Herfst, H. G. A. Huizing, P. G. Steeneken, and J. Schmitz, "Characterization of dielectric charging in RF MEMS capacitive switches," in *Proc. IEEE Int. Conf. Microelectron. Test Structures*, Mar. 2006, pp. 133–136.
[19] T. Ikehashi, T. Ohguro, E. Ogawa, H. Yamazaki, K. Kojima, M. Matsuo, K. Ishimaru, and H. Ishiuchi, "A robust RF MEMS variable capacitor with piezoelectric and electrostatic actuation," in *Proc. IEEE MTT-S Int. Microw. Symp. Dig.*, Jun. 2006, pp. 39–42.
[20] X. Yuan, Z. Peng, J. C. M. Hwang, D. Forehand, and C. L. Goldsmith, "Temperature acceleration of dielectric charging in RF MEMS capacitive switches," in *Proc. IEEE MTT-S Int. Microw. Symp. Dig.*, Jun. 2006, pp. 47–50.
[21] R. E. Leoni, III, M. S. Shirokov, J. W. Bao, and J. C. M. Hwang, "A phenomenologically based transient SPICE model for digitally modulated RF performance characteristics of GaAs MESFETs," *IEEE Trans. Microw. Theory Tech.*, vol. 49, no. 6, pp. 1180–1186, Jun. 2001.
[22] S. M. Sze, *Physics of Semiconductor Devices*, 2nd ed. New York: Wiley, 1981, pp. 259–263.

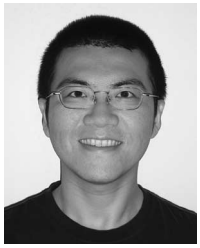

Xiaobin Yuan (S'01–M'06) was born in Beijing, China, in 1978. He received the B.E. degree in electronic engineering from Tsinghua University, Beijing, China, in 2001 and the Ph.D. degree in electrical engineering from Lehigh University, Bethlehem, PA, in 2006.

He is currently with IBM Microelectronics, Hopewell Junction, NY. His research interests include characterization and compact modeling of deep-submicrometer CMOS, RF/Microwave devices, and reliability modeling of RF microelectromechanical system (MEMS) devices.

Dr. Yuan is a member of the IEEE Electron Devices Society and Microwave Theory and Techniques Society.

Zhen Peng (S'06) was born in Shanghai, China, in 1980. He received the B.E. degree in electrical engineering from Shanghai Jiao Tong University, China, in 2003. He is currently working toward the Ph.D. degree in electrical and computer engineering at Lehigh University, Bethlehem, PA, where he is involved with RF-MEMS capacitive switches project, focusing on characterization and modeling of dielectric charging with different materials and conditions, reliability test, and research.

From 2003 to 2005, he was an IC Design Engineer with Ricoh Electronics (Shanghai) Company focusing on low-voltage analog circuit design (dc–dc converter) and reliability test.

James C. M. Hwang (M'81–SM'82–F'94) received the B.S. degree in physics from the National Taiwan University, Taipei, Taiwan, R.O.C., in 1970, and the M.S. and Ph.D. degrees in materials science and engineering from Cornell University, Ithaca, NY, in 1973 and 1976, respectively.

After 12 years of industrial experience at IBM, AT&T, GE, and GAIN, he joined the faculty of Lehigh University, Bethlehem, PA, in 1988, where he is currently a Professor of electrical engineering and the Director of the Compound Semiconductor Technology Laboratory. In 2002, he helped establish the Center for Optical Technologies at Lehigh University and served as its interim Director. He has been a Professor at Nanyang Technological University, Singapore, an Advisory Professor at Shanghai Jiaotong University, Shanghai, China, and a Consultant for the U.S. Government and many electronic companies in the areas of RF/microwave devices and integrated circuits. He was also a cofounder of GAIN and QED, with the latter one becoming a public company (IQEP). He has published approximately 200 technical papers and holds four U.S. patents.

David Forehand (M'04) received the Bachelors and Masters degrees in chemical engineering from the University of New Mexico, Albuquerque, NM.

His research involved mass spectrometry of aluminum plasma etching, which was conducted at Sandia National Laboratory's Class sub-1 cleanroom. From 1989 to 1996, he worked with Texas Instruments' (TI) Defense Systems and Electronics Group (DSEG) in Dallas, Texas, on infrared focal plane arrays (IRFPAs). He had sole responsibility for development and manufacturing of all plasma etch and plasma-enhanced chemical vapor deposition (PECVD) processes. IRFPA achievements include four patents, two trade secrets.

Mr. Forehand was a recipient of the Texas Instruments' 1995 DSEG Technical Award for Excellence. He later left TI to work for a semiconductor equipment supplier working on advanced high-density plasma (HDP) etch systems. He was the Customer Site Lead Engineer responsible for the HDP systems and training of new engineers. He returned to TI in 1998 to become part of a team in the Microcomponents Technology Center to design, develop, and produce the world's first true analog biaxial micromirror for optical switching, which is capable of aiming to $\sim$1 μrad. He is the holder of three patents and one patent pending for his optical MEMS work. In April 2001, he joined Raytheon's RF MEMS team to lead the process engineering development activity. During that time, he was responsible for transitioning processes for manufacturability and repeatability as well as developing improvements for increased reliability, which led to an additional patent. In July 2002, he helped found MEMtronics to continue the development and manufacturing of RF MEMS technology for commercial, space, and military applications. His key philosophy is that a process flow must work in production. If it does not, then the process flow is not viable regardless of its performance. Performance is for papers; production is for profits.

Charles L. Goldsmith (S'79–M'82–SM'94) received the Bachelors and Masters degrees in electrical engineering from the University of Arizona, Tucson, and the Ph.D. degree from the University of Texas at Arlington.

Since 1982, he has been involved in the design and development of microwave/millimeter-wave circuits and subsystems. He has been employed by M/A COM, Texas Instruments, and was previously an Engineering Fellow with the Raytheon Company. He formed the MEMtronics Corporation, Plano, TX, in 2001, where he is currently pursuing business opportunities for RF MEMS in the commercial and defense markets. He has been developing RF MEMS devices and circuits since 1993, and he is the Inventor of the capacitive membrane RF MEMS switch. He has spent the last decade dedicated to the development and application of this technology. These activities include the innovation of switches, phase shifters, and tunable antennas for radar and satcom applications as well as variable capacitors and tunable filters for microwave receiver front ends. He has authored or coauthored over 45 publications on microwave circuits, photonics, and RF MEMS. He is also Inventor or Coinventor of nine granted and three pending patents in related fields.

Dr. Goldsmith has been the Guest Editor for three "Special Issues on RF Applications of MEMS Technology" for the *International Journal of RF* and *Microwave Computer-Aided Engineering* (Wiley:1999, 2001, and 2004). He is a Senior Member of the IEEE Microwave Theory and Techniques Society and Electron Device Society, and a member of Tau Beta Pi. He has served as Chairman and Vice-Chairman of the IEEE LEOS Dallas Chapter and currently serves on the IEEE MTT Technical Coordinating Committee (TCC-21) on RF MEMS.